PHYSICS

Experimental realization of deep-subwavelength confinement in dielectric optical resonators

Shuren Hu[1]*, Marwan Khater[2], Rafael Salas-Montiel[3], Ernst Kratschmer[2], Sebastian Engelmann[2], William M. J. Green[2], Sharon M. Weiss[1,4]*

The ability to highly localize light with strong electric field enhancement is critical for enabling higher-efficiency solar cells, light sources, and modulators. While deep-subwavelength modes can be realized with plasmonic resonators, large losses in these metal structures preclude most practical applications. We developed an alternative approach to achieving subwavelength localization of the electric and displacement fields that is not accompanied by inhibitive losses. We experimentally demonstrate a dielectric bowtie photonic crystal structure that supports mode volumes commensurate with plasmonic elements and quality factors that reveal ultralow losses. Our approach opens the door to the extremely strong light-matter interaction regime with, simultaneously incorporating both an ultralow mode volume and an ultrahigh quality factor, that had remained elusive in optical resonators.

INTRODUCTION

Light-matter interaction in an optical resonator is enhanced through two confinement mechanisms: (i) temporal confinement, which is the photon cavity lifetime and is characterized by the quality factor (Q), and (ii) spatial confinement, which is the ability to localize light into a tightly confined space and is characterized by the modal volume (V_m). Here, the traditional definition of mode volume (V_m) is considered using Eq. 1 (where E is the electric field and ε is the permittivity), which is most strongly scaled by peak electric field energy and is most relevant for applications relying on Purcell enhancement and strongly enhanced nonlinear optical processes

$$V_m = \frac{\int \varepsilon E^2 dV}{\max(\varepsilon E^2)} \quad (1)$$

Simultaneously achieving high confinement in both categories has been a long-time pursuit in nanophotonics research and holds the promise for revolutionary advances in generating, modulating, and detecting light, including higher-efficiency light sources (*1*–*4*) and solar cells (*5*–*8*), as well as faster and lower power consumption optical switches and modulators (*9*–*13*). Plasmonic and metal-based metamaterial structures are capable of concentrating light into deep-subwavelength volumes [that is, mode volume = $V_m \sim 10^{-3}\,(\lambda/n_{air})^3$] by accessing a surface plasmon resonance (*6*, *14*, *15*). However, resistive heating losses lead to poor temporal confinement (that is, quality factor = $Q \sim 10$) and prohibit the realization of practical devices that require propagation of energy (*16*). Recent work replacing metals with all-dielectric materials has led to encouraging progress for enhanced spatial light localization through scattering in high-index dielectric nanoparticles, but the lack of an intrinsic confinement mechanism within these dielectric structures has prevented light concentration on par with plasmonics. Furthermore, the scattering mechanism in these subwavelength dielectric nanoparticles is incapable of providing temporal confinement (*17*–*19*).

Historically, low-loss dielectric structures, such as interferometers and ring resonators, have been the building blocks of photonic technologies, but they are diffraction-limited and are therefore unable to focus light below $\lambda/2n_d$, where n_d is the refractive index of the dielectric material in which the optical mode is confined. Photonic crystals have provided the best confinement in lossless dielectric materials to date (*20*). Typical photonic crystals use a simple unit cell geometry—circles or rectangles (*21*–*23*)—and have a $V_m \sim 1\,(\lambda/n_d)^3$. Slotted photonic crystal cavities can further squeeze light into a nanoscale low-index region by designing an abrupt index discontinuity along the electric field polarization direction. Slotted photonic crystal cavities reduce the V_m to ~0.01 $(\lambda/n_{air})^3$, almost two orders of magnitude lower than traditional photonic crystal cavities (*24*, *25*). However, it is difficult to achieve deeper subwavelength confinement via a slot configuration alone. In addition, because slotted photonic structures inherently confine cavity modes within a low-index region, they are not suitable for applications requiring strong light-matter interaction in high-index materials, such as silicon or many highly nonlinear optical materials.

While spatial localization of photons typically occurs due to a single physical mechanism, such as total internal reflection in waveguides and photonic bandgap confinement in photonic crystals, it is apparent from previous work that a second level of spatial localization is possible (*6*, *15*, *24*–*26*). In the case of slotted photonic crystal waveguides, light is first confined in the dielectric mode by the photonic bandgap effect such that light is spatially localized in the dielectric region between the lattice holes. Then, introduction of an air slot that cuts through the dielectric region further localizes the light within this air slot due to electromagnetic boundary conditions. Our previously reported theoretical study suggests that this two-step light confinement effect can be best exploited to achieve low mode volume by using subwavelength modifications of the photonic crystal lattice holes rather than the dielectric region between lattice holes (*26*). In that study, light is first confined in the air mode by the photonic bandgap effect such that light is spatially localized inside the lattice air holes. Then, a bowtie-shaped subwavelength dielectric inclusion added to the lattice holes enables redistribution of the optical mode to the tips of the bowtie as a result of electromagnetic boundary conditions. The two-step light localization process in photonic crystals preserves the high-Q nature of the photonic crystal cavity. A later theoretical study also found that a

[1]Department of Physics and Astronomy, Vanderbilt University, Nashville, TN 37235, USA. [2]IBM Thomas J. Watson Research Center, 1101 Kitchawan Road, Yorktown Heights, NY 10598, USA. [3]Laboratoire de Nanotechnologie et d'Instrumentation Optique, Institut Charles Delaunay CNRS-UMR 6281, Université de Technologie de Troyes, Troyes 10004, France. [4]Department of Electrical Engineering and Computer Science, Vanderbilt University, Nashville, TN 37235, USA.
*Corresponding author. Email: shuren.hu@gmail.com (S.H.); sharon.weiss@vanderbilt.edu (S.M.W.)

bowtie-shaped subwavelength dielectric inclusion in the center of a slotted photonic crystal nanobeam with a 1-nm air gap between the bowtie tips enables extremely high Q/V_m values (*27*). Here, we introduce design improvements to bowtie-shaped photonic crystal unit cells that enable additional mode confinement in the out-of-plane direction accompanied by a commensurate increase in the peak electric field strength, and we experimentally demonstrate a bowtie photonic crystal cavity with a loaded Q factor on the order of 10^5 and record deep-subwavelength mode confinement in silicon [$V_m \sim 10^{-3}\ (\lambda/n_{Si})^3$] that is verified by optical near-field measurements. This extreme light concentration is on par with plasmonic resonators, yet the low-loss dielectric material allows a concurrent ultrahigh Q factor (*26*).

RESULTS

Bowtie photonic crystal cavity design

To achieve improved out-of-plane modal confinement in the bowtie unit cell compared to our previous design of a bowtie photonic crystal, a thickness modulation is added in the bowtie tip region to form a v-groove cross-sectional profile that is experimentally realizable. Figure 1 compares the energy distribution in the v-groove bowtie unit cell to a traditional circular unit cell with and without an air slot. The extreme light localization at the bowtie tips leads to an 80-fold increase in the peak electric field amplitude compared to the circular unit cell and an eightfold increase compared to the slotted unit cell.

A silicon photonic crystal cavity is designed using the bowtie-shaped unit cell with the v-groove by slowly varying the radius of the unit cell, as shown in Fig. 2A. Because the dielectric bowtie element is inside the envelope of a traditional air hole, the photonic crystal is designed to confine the air mode such that light is localized into the air hole region and then further localized to the tips of the dielectric bowtie within the air hole region. The band diagram in Fig. 2B shows that the air mode of the bowtie photonic crystal cavity unit cell lies within the mode gap of the mirror unit cells, providing the requisite confinement for the cavity mode. The wavelength of the cavity air mode is approximately 1570 nm at the band edge [$k_x = 0.5(2\pi/a)$]. As is the case for all one-dimensional (1D) photonic crystal cavities, the Q factor of the bowtie photonic crystal cavity is governed in large part by the band gap tapering from the cavity to mirror unit cells. We choose to transition between the center and mirror unit cells in a quadratic fashion, similar to the approach followed in other high-Q photonic crystal designs (*21*–*23*).

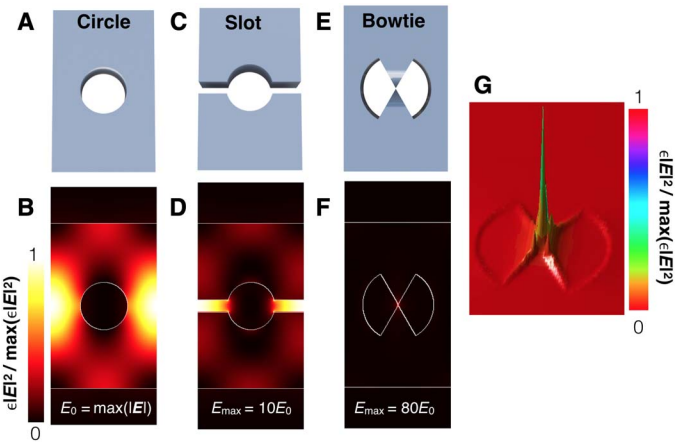

Fig. 1. Comparison of light concentration in different photonic crystal unit cells. (**A** and **B**) Traditional circular unit cell of a photonic crystal and its electric energy profile at the dielectric mode band edge. (**C** and **D**) Slotted photonic crystal unit cell and its electric energy profile at the dielectric band edge. (**E** and **F**) Bowtie photonic crystal unit cell and its electric energy profile at the air band edge. The tip of the v-groove is modeled to extend down to the middle of the silicon slab. (**G**) 3D profile of the mode in the bowtie unit cell showing the electric energy distribution. All profiles are taken at the middle of the silicon slab. All color maps are scaled according to the minimum and maximum electrical energy values of each individual unit cell. The maximum electric field amplitude in each unit cell scales as follows: traditional circular unit cell = 1 (normalized), slotted unit cell = 10, bowtie unit cell = 80.

Figure 2 (C and D) shows the top and side view profiles of the optical mode in the center cavity unit cell, and the electric energy (proportional to εE^2) across the bowtie photonic crystal cavity is shown in Fig. 2 (E and F) and fig. S2 (A and B). We note that, because the dimensions of the bowtie photonic crystal are the same for all simulations, the electric energy is directly proportional to electric energy density. In this simulation, there are 20 tapering unit cells between the central cavity unit cell and the 10 mirror unit cells on each side of the cavity; not all unit cells are shown in the figures. The mode is highly confined between the bowtie tips in the central cavity unit cell (fig. S2, C and D) and decays gradually into the mirror segments, giving a Gaussian-shaped electric energy profile that minimizes radiation losses (fig. S2E). At the resonance wavelength of λ = 1561.12 nm, the simulated Q factor is 6.55×10^6. The V_m is calculated to be $6.09 \times 10^{-4}\ \mu m^3$ using Eq. 1. Given the small dimensions of the bowtie tip, the mode extends partially in air and partially in silicon. Hence, the normalized mode volume should fall between that of the mode volume normalized to the wavelength in silicon [$V_m = 6.7 \times 10^{-3}\ (\lambda/n_{Si})^3$] and the mode volume normalized to the wavelength in air [$V_m = 1.6 \times 10^{-4}\ (\lambda/n_{air})^3$]. This mode volume is about two orders of magnitude smaller than those of other photonic crystal cavities, as shown in table S1 (*22*–*24*, *28*, *29*).

Fabricated bowtie photonic crystal cavity and measured *Q* factor

Figure 3A shows a scanning electronic microscope (SEM) image of the fabricated bowtie photonic crystal with 20 tapering unit cells and 10 mirror unit cells on each side of the central cavity unit cell. The width of the bowtie tip connection is estimated to be approximately 12 nm (Fig. 3B). Given that there are only a few pixels comprising the bowtie tip, this value has a relatively large error bar of ±5 nm. The bowtie angle is estimated to be approximately 57°. The radii of center and mirror unit cells are measured to be 147 and 190 nm, respectively. The width of waveguide is measured to be 691 nm. Figure 3C shows a titled SEM image that reveals the v-shaped structure at the bowtie tip; the unit cells shown in this image are from a photonic crystal fabricated by the same process as the one in Fig. 3A but released from the oxide substrate using a buffered hydrofluoric acid etch. Transmission measurements carried out on the bowtie photonic crystal show that the fundamental mode at λ_r = 1578.85 nm has a loaded Q of approximately 1×10^5 (Fig. 3D). The modes supported by the photonic crystal are located near the short wavelength band edge (~1520 nm), which is consistent with design (Figs. 2B and 3D). The transmission intensity of the resonance peaks is low compared to that of the band edge (fig. S3) due to the high mirror confinement in the cavity. We anticipate that higher Q resonances can be designed and measured by using alternate coupling techniques

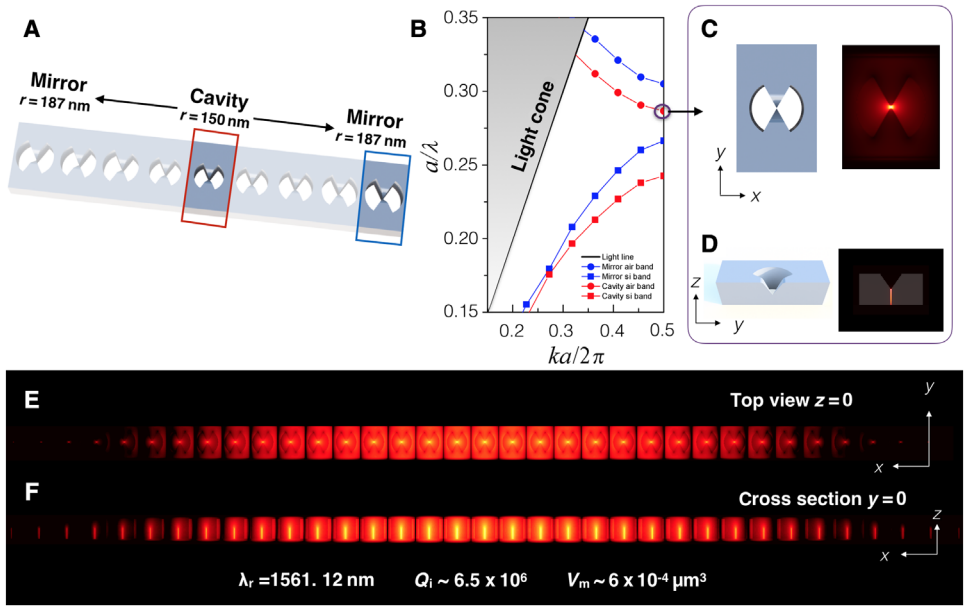

Fig. 2. Design of silicon photonic crystal using a bowtie-shaped unit cell. (**A**) The cavity is formed with a center unit cell of 150 nm radius and mirror unit cells of 187 nm radii on both sides of the cavity. The radius is gradually tapered from the center to the mirror segments. The photonic crystal lattice spacing is a = 450 nm, and the width of the waveguide is 700 nm. The structure is designed with a 220-nm silicon device layer and a 2-μm-thick buried oxide layer. (**B**) Optical band structures of the cavity unit cell (red curve) and mirror unit cell (blue curve). (**C**) Top view (*xy* plane) and (**D**) cross-sectional view (*yz* plane) schematics and associated air band edge electrical energy in the center unit cell. (**E**) Log plot of the photonic crystal cavity electric energy distribution at the resonance wavelength in the *xy* plane at z = 0 (v-groove tip). (**F**) Log plot of the photonic crystal cavity electric energy distribution at the resonance wavelength in the *xz* plane at y = 0 (bowtie tip). Figure S2 (A and B) shows the same mode profiles using a linear scale.

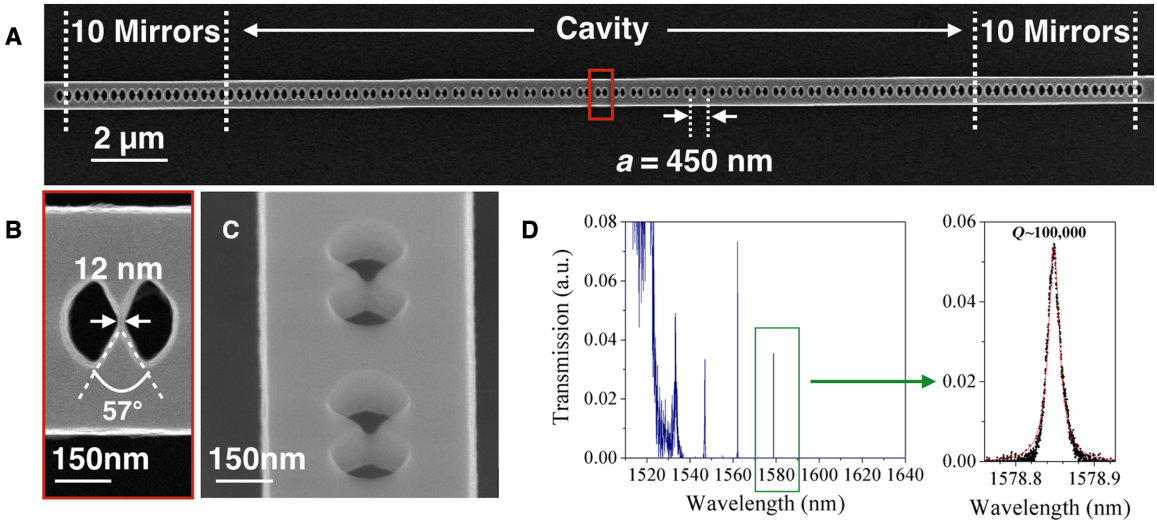

Fig. 3. Transmission of fabricated bowtie photonic crystal. (**A**) SEM image of the bowtie photonic crystal. (**B**) Zoomed-in image of a single unit cell in the red box in (A). (**C**) Tilted SEM image of an undercut bowtie photonic crystal revealing the out-of-plane profile. (**D**) Measured transmission spectrum. The fundamental mode has Q ~ 100,000 at λ = 1578.85 nm. The second-order and third-order peaks are located at 1562.20 and 1546.96 nm, with Q factors of 21,800 and 5156, respectively. a.u., arbitrary units.

that allow light to be coupled directly into the cavity instead of first passing through the mirror unit cells (for example, side coupling or evanescent coupling from a fiber).

Near-field measurements

To experimentally verify the simulated optical field distribution of the bowtie photonic crystal resonators, we used apertureless near-field scanning optical microscopy (NSOM) to probe the resonance mode. Considering the practical constraints of the NSOM system, the structure shown in Fig. 3 is not ideal for NSOM measurements due to the narrow resonance linewidth (~15 pm) and low transmission intensity (~0.04). Accordingly, a bowtie photonic crystal is designed and fabricated with reduced mirror confinement (five mirror unit cells on each side of the cavity) to increase both the linewidth (~50 pm)

and transmission intensity (~0.2), as shown in fig. S4. Because the mode is tightly confined in the cavity, the mode volume is not changed by reducing the number of mirror unit cells ($V_m = 6.09 \times 10^{-4}$ μm^3 for five mirror unit cells). Consequently, conclusions drawn from NSOM measurements on the five-mirror unit cell bowtie photonic crystal are also applicable to the higher Q cavities with additional mirror unit cells. The NSOM operates in a tapping mode in which the tip oscillates from 0 to 30 nm above the sample surface. Therefore, the near field measured by the NSOM does not directly correspond to the calculated mode volume within the bowtie (Fig. 2E). To correlate experiment and simulation, we simulate the electric energy localization in the central unit cell of bowtie photonic crystal at 15 nm above the silicon surface as an estimate of the expected average scattering field that can be detected by the NSOM (Fig. 4A). The calculated size of the electric energy localization, which is estimated by the full width at half maximum (FWHM) of the electric energy distribution in the unit cell, linearly increases from the center of the silicon slab (fig. S5) and is estimated to be ~183 nm along the y direction and 143 nm along the x direction at a distance of 15 nm above the silicon surface. Figure 4 (B and C) shows the atomic force microscope (AFM) topology and simultaneously measured optical near-field mapping of the bowtie photonic crystal cavity, respectively. The shape of the bowties shown in Fig. 4B is distorted due to the resolution limit of the AFM mode of the NSOM when measuring bowtie features that reside below the surface of the sample using a tapping mode above the surface of the sample. The SEM image shown in the inset of Fig. 4B reveals the actual shape of one of the bowtie unit cells in this sample. The measured electric energy (Fig. 4C) is confined at the bowtie tips, in agreement with the simulated electric energy (Fig. 4A) distribution in the cavity. Figure 4 (D and E) shows the measured electric energy profiles along x and y slices of the central unit cell. We identify the silicon region as the shaded area in Fig. 4 (D and E), based on AFM measurements (Fig. 4, D and E, dotted line). The simulated electric energy profiles are shown by the blue curves in Fig. 4 (D and E). The NSOM-measured profile (red markers) along the y slice through the center of the cavity shows a sharp tip of the field at the bowtie center, indicating a concentrated electric energy. The size is estimated to be ~175 nm by considering the FWHM of the electric energy distribution in the central cavity unit cell, which is in agreement with simulation. The NSOM-measured field profile along the x slice through the center of the cavity has an FWHM of ~267 nm. We attribute

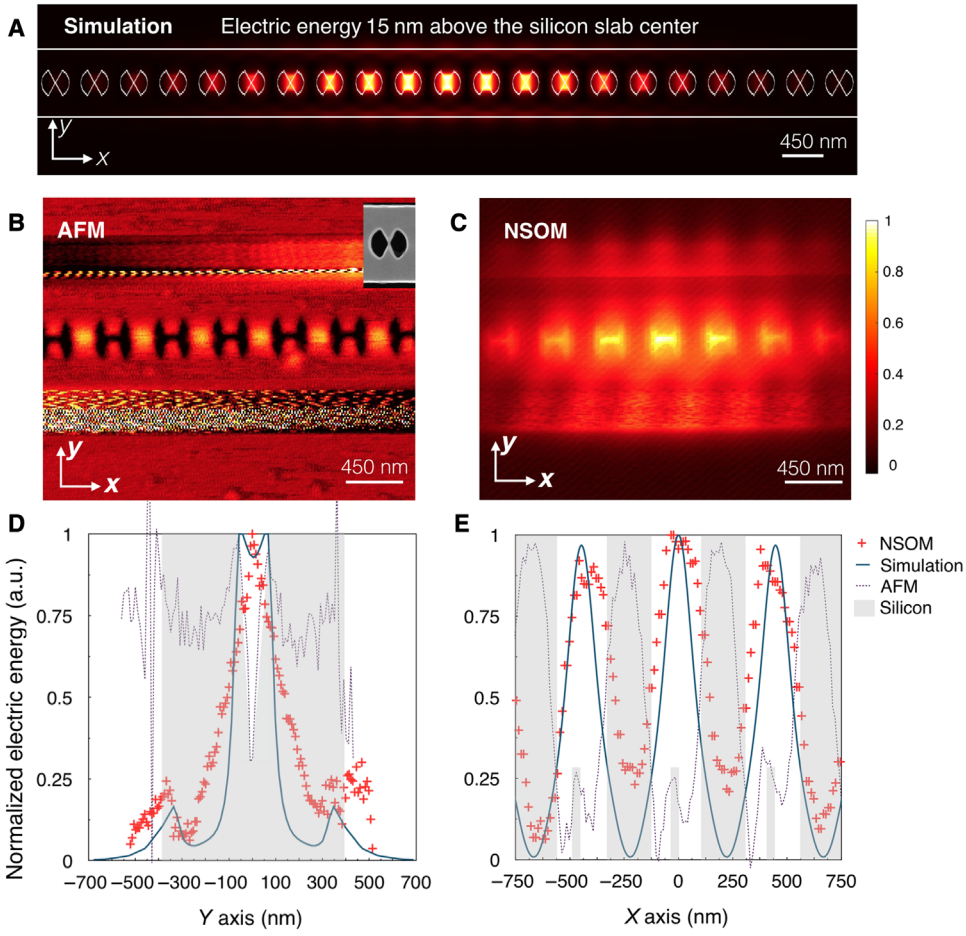

Fig. 4. Analysis of spatial confinement via NSOM measurements. (**A**) Schematic of bowtie photonic crystal cavity with overlay of simulated electric energy 15 nm above the silicon surface, where the NSOM measures the scattered field. (**B**) AFM measurement and (**C**) corresponding electric energy distribution, as measured by NSOM. The inset in (B) shows a higher-resolution SEM image of one of the bowtie unit cells from the measured cavity. (**D** and **E**) Simulated and NSOM-measured near-field profile along the y direction and x direction, respectively, along with superimposed AFM line scan.

the discrepancy between the experimental and simulation results to a combination of the influence of the NSOM tip itself on the electric energy distribution and to the fact that NSOM preferably detects the E_z signal, while the photonic crystal is designed for transverse electric (TE)–polarized light (that is, mainly E_y component). We note that the measured dimensions of the electric energy localization along the x and y directions of the bowtie photonic crystal are within a factor of 2 of those of plasmonic resonators measured using NSOM systems, as shown in table S2 (*14*, *30*, *31*). Moreover, although the field distribution for the bowtie photonic crystal and plasmonic bowties is different, the calculated mode volume, which, in the case of the photonic crystal, spans multiple unit cells, is nearly identical.

DISCUSSION

Our work demonstrates that a dielectric resonator can serve as a promising alternative to lossy metals for extreme light concentration and manipulation. Further optimization of the design and fabrication parameters may lead to bowtie photonic crystals with an even higher Q/V_m ratio. We believe that our work provides two specific contributions for future research. First, it showcases the power of combining subwavelength dielectric structure with photonic band theory. Engineering the photonic bandgap overcomes the challenges encountered while confining optical modes in nanoscatterers, enabling the design of nanoscatterers that are able to precisely adjust the optical mode distributions at subwavelength scales. Second, we prove that it is possible in a single, low-loss structure to achieve a mode volume commensurate with plasmonic elements while maintaining a quality factor that is characteristic of traditional photonic crystal cavities. Such an unprecedented strong light-matter interaction platform can facilitate the advancement of science in a broad range of applications, including low-power optoelectronics (*1*, *3*, *4*, *9*–*12*), nonlinear optics (*6*, *13*, *20*), and quantum optics (*32*, *33*).

MATERIALS AND METHODS

Finite-difference time-domain simulations

The numerical simulations presented in this study were carried out with three-dimensional finite-difference time-domain (FDTD) analysis using commercial software, Lumerical FDTD (Lumerical Solutions Inc.). The band structures and mode profiles of the unit cells in Fig. 2 were calculated using FDTD. The center xy plane of the silicon slab was defined as the $z = 0$ plane, and the bowtie tip of the central unit cell was defined as the origin point $x = 0$, $y = 0$ in the paper. The photonic crystal lattice spacing is $a = 450$ nm, and the width of the waveguide is 700 nm. The radius of the center unit cell is 150 nm, and the radii of the mirror unit cells are 187 nm. The bowtie tip angle is designed to be 60°. The out-of-plane height of the bowtie tip center is defined to be half of the thickness of the silicon slab to be consistent with the dimensions of the fabricated structures. The bowtie height is linearly tapered over an in-plane distance equal to 75 nm such that the vertical angle is 34° (see Figs. 2D and 3C). The mesh size within the photonic crystal lattice holes was chosen to be a uniform 4 nm per grid, while the remainder of the simulation space is meshed by the Lumerical default conformal mesh. For the cavity simulation, symmetric boundary conditions were applied along the x direction, and antisymmetric boundary conditions were applied along the y direction to reduce the calculation time. The source was defined as a magnetic dipole H_z at the (225 nm, 0 nm, 0 nm) coordinate.

Photonic crystal design

The photonic crystal tapering follows the quadratic tapering

$$r_i = r_0\left(1 + \left(\frac{i}{m}\right)^2\right) \tag{2}$$

where

$$m = \frac{N_c}{\sqrt{\frac{r_m}{r_0} - 1}} \tag{3}$$

In the above expressions, r_0 and r_m are the radii of the cavity and mirror unit cells, respectively, and N_c is the number of taper unit cells on each side of the cavity. In our design, $r_0 = 150$ nm, $r_m = 187$ nm, $N_c = 20$, and there are 10 mirror unit cells on each side of the cavity. Transmission measurements become challenging for a larger number of taper unit cells or larger number of mirror unit cells as the intensity of the fundamental mode approaches the noise floor.

Fabrication

The photonic crystals were fabricated on 8-inch silicon-on-insulator wafers with a 220-nm device layer and 2-μm-thick buried oxide layer (Soitec) using an electron beam lithography process on a Leica VB6-HR 100kV system. We note that, to obtain the v-groove shape at the bowtie tip, a dose gradient was manually assigned to create a grayscale height profile in the electron beam photoresist. After patterns were transferred to the device layer through a reactive ion etch process, a second lithography step was carried out to define an SU8 polymer mode coupler. The SU8 coupler was designed to be 3 μm wide and 2 μm thick to match the optical mode of the lensed fiber tip.

To attain a high-resolution SEM image of the v-groove at the bowtie tip center, an undercut process was performed to remove the buried oxide layer on one of the bowtie photonic crystal samples. For the undercut procedure, an additional lithography step was carried out to open a window for the undercut region. The sample was soaked in buffered oxide etchant (10:1) for 20 min to etch away approximately 1 μm of the buried oxide layer.

Measurements

In preparation for optical measurements, samples were cleaved across each end of the bus waveguide, several millimeters away from the central device, and mounted on an XY positioning stage. Piezo-controlled XYZ stages were used to position and couple light to/from polarization-maintaining lensed fibers (OZ Optics Ltd.). A tunable continuous-wave laser (Santec TSL-510) was used to perform passive transmission measurements, using quasi-TE polarization, over the wavelength range of 1500 to 1630 nm.

For the optical near-field measurements, a high-quality etched silicon AFM probe (Bruker TESPA-V2) with a nominal tip radius of 8 nm was put in intermittent contact at a frequency f_0 near the surface of the samples. The changes in the in-line transmission measurements due to the intermittent perturbation of the optical mode by the AFM probe were recorded with a near-infrared high-sensitivity avalanche photodetector (APD module Hamamatsu C5460SPL) and demodulated with a lock-in amplifier locked at a frequency f_0. The transmitted signal is related to the amplitude squared of the local electric near field

normalized to the power carried by the optical mode. An optical image is constructed based on the demodulated in-line transmission measurements as the AFM probe raster scans the sample (scan direction is *x* direction) at an average distance of 15 nm from its surface. A topography image was recorded simultaneously to the optical near-field image. A tunable continuous wave laser (Photonetics Tunics ECL 1560) was used to perform the in-line transmission measurements, using quasi-TE polarization, over the wavelength range of 1500 to 1630 nm.

SUPPLEMENTARY MATERIALS

Supplementary material for this article is available at http://advances.sciencemag.org/cgi/content/full/4/8/eaat2355/DC1

Fig. S1. Design of photonic crystal cavity in an FDTD simulation.

Fig. S2. Resonance mode profile.

Fig. S3. Broadband transmission spectrum of bowtie photonic crystal cavity shown in Fig. 3D.

Fig. S4. SEM image and transmission of the bowtie photonic crystal cavity characterized by NSOM.

Fig. S5. Position-dependent electric energy distribution in the central cavity unit cell of the silicon bowtie photonic crystal.

Table S1. Calculated mode volume (V_m) and measured quality factor (Q) of different photonic crystal (PhC) cavities including the bowtie photonic crystal cavity presented in this work.

Table S2. NSOM-measured mode sizes of plasmonic structures in comparison to dielectric bowtie photonic crystal reported in this work.

REFERENCES AND NOTES

1. S. Noda, M. Fujita, T. Asano, Spontaneous-emission control by photonic crystals and nanocavities. *Nat. Photonics* **1**, 449–458 (2007).
2. R. F. Oulton, V. J. Sorger, T. Zentgraf, R.-M. Ma, C. Gladden, L. Dai, G. Bartal, X. Zhang, Plasmon lasers at deep subwavelength scale. *Nature* **461**, 629–632 (2009).
3. H. Altug, D. Englund, J. Vučković, Ultrafast photonic crystal nanocavity laser. *Nat. Phys.* **2**, 484–488 (2006).
4. S. Matsuo, A. Shinya, T. Kakitsuka, K. Nozaki, T. Segawa, T. Sato, Y. Kawaguchi, M. Notomi, High-speed ultracompact buried heterostructure photonic-crystal laser with 13 fJ of energy consumed per bit transmitted. *Nat. Photonics* **4**, 648–654 (2010).
5. H. A. Atwater, A. Polman, Plasmonics for improved photovoltaic devices. *Nat. Mater.* **9**, 205–213 (2010).
6. J. A. Schuller, E. S. Barnard, W. Cai, Y. Chul Jun, J. S. White, M. L. Brongersma, Plasmonics for extreme light concentration and manipulation. *Nat. Mater.* **9**, 193–204 (2010).
7. M. A. Green, S. Pillai, Harnessing plasmonics for solar cells. *Nat. Photonics* **6**, 130–132 (2012).
8. M. L. Brongersma, Y. Cui, S. H. Fan, Light management for photovoltaics using high-index nanostructures. *Nat. Mater.* **13**, 451–460 (2014).
9. G. T. Reed, G. Mashanovich, F. Y. Gardes, D. J. Thomson, Silicon optical modulators. *Nat. Photonics* **4**, 518–526 (2010).
10. Q. Xu, B. Schmidt, S. Pradhan, M. Lipson, Micrometre-scale silicon electro-optic modulator. *Nature* **435**, 325–327 (2005).
11. J. C. Rosenberg, W. M. Green, S. Assefa, D. M. Gill, T. Barwicz, M. Yang, S. M. Shank, Y. A. Vlasov, A 25 Gbps silicon microring modulator based on an interleaved junction. *Opt. Express* **20**, 26411–26423 (2012).
12. A. Melikyan, L. Alloatti, A. Muslija, D. Hillerkuss, P. C. Schindler, J. Li, R. Palmer, D. Korn, S. Muehlbrandt, D. Van Thourhout, B. Chen, R. Dinu, M. Sommer, C. Koos, M. Kohl, W. Freude, J. Leuthold, High-speed plasmonic phase modulators. *Nat. Photonics* **8**, 229–233 (2014).
13. K. Nozaki, T. Tanabe, A. Shinya, S. Matsuo, T. Sato, H. Taniyama, M. Notomi, Sub-femtojoule all-optical switching using a photonic-crystal nanocavity. *Nat. Photonics* **4**, 477–483 (2010).
14. Y. Luo, M. Chamanzar, A. Apuzzo, R. Salas-Montiel, K. N. Nguyen, S. Blaize, A. Adibi, On-chip hybrid photonic–plasmonic light concentrator for nanofocusing in an integrated silicon photonics platform. *Nano Lett.* **15**, 849–856 (2015).
15. M.-K. Kim, H. Sim, S. Ju Yoon, S.-H. Gong, C. Won Ahn, Y.-H. Cho, Y.-H. Lee, Squeezing photons into a point-like space. *Nano Lett.* **15**, 4102–4107 (2015).
16. J. C. Ndukaife, V. M. Shalaev, A. Boltasseva, Plasmonics—Turning loss into gain. *Science* **351**, 334–335 (2016).
17. J. Yan, P. Liu, Z. Lin, H. Wang, H. Chen, C. Wang, G. Yang, Directional Fano resonance in a silicon nanosphere dimer. *ACS Nano* **9**, 2968–2980 (2015).
18. R. M. Bakker, D. Permyakov, Y. Feng Yu, D. Markovich, R. Paniagua-Domínguez, L. Gonzaga, A. Samusev, Y. Kivshar, B. Luk'yanchuk, A. I. Kuznetsov, Magnetic and electric hotspots with silicon nanodimers. *Nano Lett.* **15**, 2137–2142 (2015).
19. R. Regmi, J. Berthelot, P. M. Winkler, M. Mivelle, J. Proust, F. Bedu, I. Ozerov, T. Begou, J. Lumeau, H. Rigneault, M. F. García-Parajó, S. Bidault, J. Wenger, N. Bonod, All-dielectric silicon nanogap antennas to enhance the fluorescence of single molecules. *Nano Lett.* **16**, 5143–5151 (2016).
20. A. F. Koenderink, A. Alù, A. Polman, Nanophotonics: Shrinking light-based technology. *Science* **348**, 516–521 (2015).
21. E. Kuramochi, H. Taniyama, T. Tanabe, K. Kawasaki, Y.-G. Roh, M. Notomi, Ultrahigh-*Q* one-dimensional photonic crystal nanocavities with modulated mode-gap barriers on SiO_2 claddings and on air claddings. *Opt. Express* **18**, 15859–15869 (2010).
22. Q. Quan, P. B. Deotare, M. Loncar, Photonic crystal nanobeam cavity strongly coupled to the feeding waveguide. *Appl. Phys. Lett.* **96**, 203102 (2010).
23. Q. Quan, M. Loncar, Deterministic design of wavelength scale, ultra-high Q photonic crystal nanobeam cavities. *Opt. Express* **19**, 18529–18542 (2011).
24. P. Seidler, K. Lister, U. Drechsler, J. Hofrichter, T. Stöferle, Slotted photonic crystal nanobeam cavity with an ultrahigh quality factor-to-mode volume ratio. *Opt. Express* **21**, 32468–32483 (2013).
25. J. D. Ryckman, S. M. Weiss, Low mode volume slotted photonic crystal single nanobeam cavity. *Appl. Phys. Lett.* **101**, 071104 (2012).
26. S. Hu, S. M. Weiss, Design of photonic crystal cavities for extreme light concentration. *ACS Photonics* **3**, 1647–1653 (2016).
27. H. Choi, M. Heuck, D. Englund, Self-similar nanocavity design with ultrasmall mode volume for single-photon nanolinearities. *Phys. Rev. Lett.* **118**, 223605 (2017).
28. Y. Akahane, T. Asano, B.-S. Song, S. Noda, High-*Q* photonic nanocavity in a two-dimensional photonic crystal. *Nature* **425**, 944–947 (2003).
29. B.-S. Song, S. Noda, T. Asano, Y. Akahane, Ultra-high-*Q* photonic double-heterostructure nanocavity. *Nat. Mater.* **4**, 207–210 (2005).
30. A. Apuzzo, M. Février, R. Salas-Montiel, A. Bruyant, A. Chelnokov, G. Lérondel, B. Dagens, S. Blaize, Observation of near-field dipolar interactions involved in a metal nanoparticle chain waveguide. *Nano Lett.* **13**, 1000–1006 (2013).
31. V. A. Zenin, A. Andryieuski, R. Malureanu, I. P. Radko, V. S. Volkov, D. K. Gramotnev, A. V. Lavrinenko, S. I. Bozhevolnyi, Boosting local field enhancement by on-chip nanofocusing and impedance-matched plasmonic antennas. *Nano Lett.* **15**, 8148–8154 (2015).
32. T. G. Tiecke, J. D. Thompson, N. P. de Leon, L. R. Liu, V. Vuletić, M. D. Lukin, Nanophotonic quantum phase switch with a single atom. *Nature* **508**, 241–244 (2014).
33. A. Sipahigil, R. E. Evans, D. D. Sukachev, M. J. Burek, J. Borregaard, M. K. Bhaskar, C. T. Nguyen, J. L. Pacheco, H. A. Atikian, C. Meuwly, R. M. Camacho, F. Jelezko, E. Bielejec, H. Park, M. Lončar, M. D. Lukin, An integrated diamond nanophotonics platform for quantum optical networks. *Science* **354**, 847–850 (2016).

Acknowledgments: We thank G. Gaur, K. J. Miller, C. Xiong, and J. S. Orcutt for helpful discussions. The photonic crystal bowtie cavities were fabricated in the Microelectronics Research Laboratory (MRL) at the IBM Thomas J. Watson Research Center. We are grateful to the MRL staff for their contributions to the success of this work. Simulations presented in this work were conducted in part using the resources of the Advanced Computing Center for Research and Education at Vanderbilt University (Nashville, TN). Additional computations were carried out with the resources of the HPC Center of Champagne-Ardenne ROMEO. Equipment and technical support in the Vanderbilt Institute for Nanoscale Science and Engineering and French regional nanofabrication and nanocharacterization platform (Nano'Mat) were also used for this work. **Funding:** This work was supported in part by the NSF (ECCS1407777). **Author contributions:** S.H. conceived the idea. M.K., E.K., and S.E. fabricated the structure. S.H. performed the transmission experiments and carried out the simulations. R.S.-M. performed the NSOM measurements. W.M.J.G. and S.M.W. advised on the several aspects of theory and experiments and supervised the overall research effort. S.H. and S.M.W. wrote the manuscript with input from all authors. **Competing interests:** The authors declare that they have no competing interests. **Data and materials availability:** All data needed to evaluate the conclusions in the paper are present in the paper and/or the Supplementary Materials. Additional data related to this paper may be requested from the authors.

Submitted 6 February 2018
Accepted 18 July 2018
Published 24 August 2018
10.1126/sciadv.aat2355

Citation: S. Hu, M. Khater, R. Salas-Montiel, E. Kratschmer, S. Engelmann, W. M. J. Green, S. M. Weiss, Experimental realization of deep-subwavelength confinement in dielectric optical resonators. *Sci. Adv.* **4**, eaat2355 (2018).